

# Brain MRA 3D Skeleton Extraction Based on Normal Plane Centroid Algorithm

Guoying Feng<sup>1</sup>, Jie Zhu<sup>2,\*</sup> and Jun Li<sup>3</sup>

1. College of Basic Medicine Binzhou Medical University, Yantai 264003, Shandong, China

2. Center of Network Information Binzhou Medical University, Yantai 264003, Shandong, China

3. Department of Medical Imaging Yantai Affiliated Hospital Binzhou Medical University, Yantai 264100, Shandong, China

## Abstract

**INTRODUCTION:** Analysis of magnetic resonance angiography image data is crucial for early detection and prevention of stroke patients. Extracting the 3D Skeleton of cerebral vessels is the focus and difficulty of analysis.

**OBJECTIVES:** The objective is to remove other tissue components from the vascular tissue portion of the image with minimal loss by reading MRA image data and performing processing processes such as grayscale normalization, interpolation, breakpoint detection and repair, and image segmentation to facilitate 3D reconstruction of cerebral blood vessels and the reconstructed vascular tissues make extraction of the Skeleton easier.

**METHODS:** Considering that most of the existing techniques for extracting the 3D vascular Skeleton are corrosion algorithms, machine learning algorithms require high hardware resources, a large number of learning and test cases, and the accuracy needs to be confirmed, an average plane center of mass computation method is proposed, which improves the average plane algorithm by combining the standard plane algorithm and the center of mass algorithm.

**RESULTS:** Intersection points and skeleton breakpoints on the Skeleton are selected as critical points and manually labeled for experimental verification, and the algorithm has higher efficiency and accuracy than other algorithms in directly extracting the 3D Skeleton of blood vessels.

**CONCLUSION:** The method has low hardware requirements, accurate and reliable image data, can be automatically modeled and calculated by Python program, and meets the needs of clinical applications under information technology conditions.

**Keywords:** MRA, average plane centroid algorithm, 3D reconstruction, skeleton extraction

Received on 27 March 2023, accepted on 13 November 2023, published on 22 November 2023

Copyright © 2023 Feng *et al.*, licensed to EAI. This open-access article is distributed under the terms of the [CC BY-NC-SA 4.0](https://creativecommons.org/licenses/by-nc-sa/4.0/), which permits copying, redistributing, remixing, transforming, and building upon the material in any medium so long as the original work is properly cited.

doi: 10.4108/eetpht.9.4450

\*Corresponding Author. Email: [jzhued@bzmc.edu.cn](mailto:jzhued@bzmc.edu.cn)

## 1. Introduction

With software and hardware technology development, medical imaging equipment has also been widely used in hospitals and rehabilitation institutions of different sizes. Among them, NMR [1] is favored by doctors and patients in the diagnosis of cerebrovascular diseases due to its unique imaging principle, no ionizing radiation, no skeletal artifacts, high resolution, multi-directional and

multi-sequence imaging, and vascular imaging without the use of contrast agents. "cerebrovascular accident" (CVA), also known as "cerebral stroke" (cerebral stroke), "stroke," is due to the blockage of blood vessels in the brain resulting in poor blood flow or because of the sudden rupture of blood vessels and brain tissue damage disease. The incidence and prevalence of stroke remain high in the world. The survey found that from November 2018 to December 2021, the incidence of stroke in China was about 28 million for men and 18 million for women [2], and the number was still increasing, among which

ischemic stroke accounted for 60%-80% of strokes, higher than the incidence of hemorrhagic stroke. Stroke has become the first cause of death in China and the leading cause of disability in adults [3-4]. Therefore, most extensive and medium-sized hospitals in China have set up special stroke centers. For the diagnosis and treatment of stroke, due to the lack of effective treatment means, prevention is currently considered to be the best measure, and early detection and diagnosis can guide patients to take preventive measures in advance to save their health and lives.

In recent years, imaging technology has made significant progress [5]. The imaging clarity of Magnetic Resonance Angiography (MRA), CT angiography (CTA), and other images is getting higher and higher. The analysis effect of vascular diseases is also improving, especially the early analysis effect of stroke caused by cerebrovascular is more significant. By analyzing brain MRA, CTA, and other image data, it is of great significance to obtain the analysis results of cerebrovascular changes, search the lesion area of stroke, and guide the early clinical diagnosis of stroke in patients. Compared with CTA, MRA imaging does not require a contrast agent and has no damage to subjects. Brain MRA examination can be used as a physical screening item in middle-aged and older adults, so the importance of quantitative analysis of MRA imaging is self-evident.

## 2. Results

Vascular skeleton extraction is a necessary step in the quantitative analysis of MRA image data. Because most of the existing skeleton extraction algorithms are two-dimensional (also known as binary image thinning), 3D image skeleton extraction algorithms are relatively few and are mainly classified as corrosion algorithms, including the iterative thinning method used by MASSEY et al. [6]. The minimum path method proposed by JIN et al. [7] and other machine learning methods emerged with the development of artificial intelligence technology—however, the precision of corrosion algorithm refinement in this method is needed. The deep learning algorithm proposed by WAGNER et al. [8] requires many case models, high requirements on hardware resources, expensive Graphics Processing Unit (GPU) cards, and large resource consumption.

Under the same hardware and software conditions, the improved average plane centroid algorithm has apparent advantages in efficiency and accuracy compared with the corrosion algorithm and machine learning algorithm to extract the three-dimensional Skeleton of MRA blood vessels. This method's defect is that the early stage preprocessing process will cause specific errors. With the development of artificial intelligence technology, the machine processing speed increases. In addition, in the case of using a large number of samples for deep learning, the machine learning algorithm has more room for improvement. The next step that must be verified is

improving the hardware configuration. The effect will be better if the machine learning algorithm is combined with the average plane centroid algorithm to extract the Skeleton of three-dimensional images. Through the use of three-dimensional vascular Skeleton, the cross-sectional area of each section of blood vessel can be reshaped, the changes of vascular cross section can be more intuitively understood, the narrow and dilated weak areas of blood vessels can be accurately located, and the relationship between brain region and changes in cerebrovascular blood supply can be analyzed in combination with the brain structure data of MRIT1, which is of great significance for guiding the prevention of cerebrovascular diseases in patients, especially in the middle-aged and elderly.

## 3. Materials and methods

To extract vascular Skeleton from brain MRA data, image data must be removed first, the coordinate system must be transformed, image preprocessing must be carried out, noise, bone, and other tissue interference factors can be eliminated, pure blood vessels and single background images can be obtained, and then the vascular Skeleton can be extracted.

### 3.1 Image transformation

#### 3.1.1 Reading data

Image data transformation refers to the original image data after processing it into a standard image file and adjusting the accuracy of the three dimensions to facilitate the following calculation process. Image transformation includes normalization (normalization of the check value to the 0-255 image space), interpolation processing (to make the accuracy of the sagittal, coronal, and axial directions of the image data consistent), breakpoint detection and repair (to supplement some pixel abnormalities or missing caused by noise, etc.) and other processing processes. The above process is also called image preprocessing in image analysis.

MRA original image data (dicom format file) includes header and image data. As shown in Figure 1, image processing needs to read out part of the image. The Python pydicom package or SimpleITK reads the dicom file and extracts part of the image data.

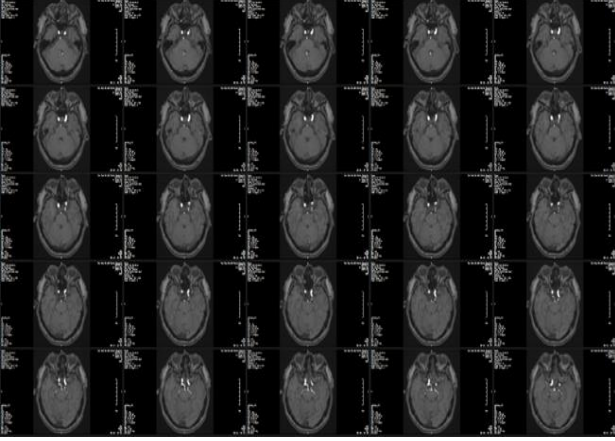


Figure 1 Raw imaging data of brain MRA  
Randomly select a subject case, use the onis2.5 software to open the header file data and 2D image of the original image file that displays the case, and capture some photos for display.

### 3.1.2 Data normalization

Data normalization usually converts data in different ranges into the same data range to facilitate subsequent analysis and processing. It is an essential data preprocessing method. There are many methods for data normalization, including maximum and minimum value methods, Z-score methods, decimal scaling methods, logarithmic function methods, and deviation standardization methods [9,10]. Most normalization methods are based on the need to normalize the value to between 0 and 1 or -1 and 1. The value of image data is usually between -1000 and 1000. Figure 2 shows the selected window width and position data during image inspection. It can be seen from the figure that the maximum pixel value of MRA image data with the adjusted window width and window position is 658, and the minimum pixel value is 0. Here, the improved max-min method is used, as shown in equation (1), to convert the pixel values of 0~658 to the gray level of 0~255, that is, 256 color levels, to become the image data that genuinely meets the image standard, as shown in Figure 3.

[Group,Element]	Title	Value
[0028:0002]	Samples per Pixel	1
[0028:0004]	Photometric Interpretation	MONOCHROME2
[0028:0010]	Rows	512
[0028:0011]	Columns	464
[0028:0030]	Pixel Spacing	0.390625\0.390625
[0028:0100]	Bits Allocated	16
[0028:0101]	Bits Stored	12
[0028:0102]	High Bit	11
[0028:0103]	Pixel Representation	0
[0028:0106]	Smallest Image Pixel Value	0
[0028:0107]	Largest Image Pixel Value	658
[0028:1050]	Window Center	184
[0028:1051]	Window Width	447
[0028:1055]	Window Center_Width Explanatio	Algo1

Figure 2 MRA image data with adjusted window width and window level

Select a window width of 447 and a window center of 447. After changing the window width and window level, the maximum pixel value of the MRA image data is 658, the minimum pixel value is 0, and the scanning accuracy voxel value is 0.390625\0.390625. Use the onis2.5 software to open and display the header file data of the case and take a partial display.

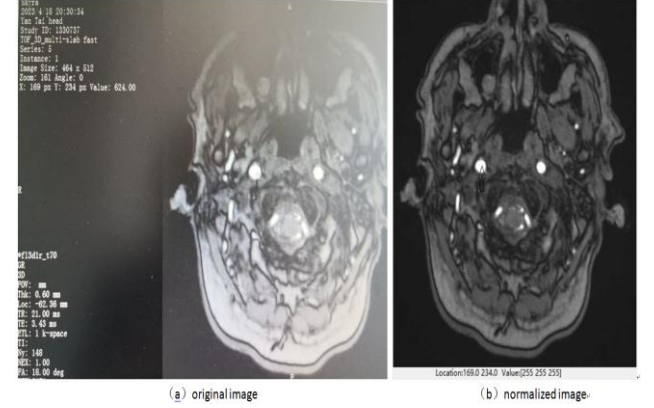


Figure 3 Comparison of images before and after normalization processing

Through image normalization, the voxel values of the image data, in this case, changed from 0-658 to 0-255, indicating a significant increase in edge clarity from the image.

$$x_{new} = 255 \times \frac{x - x_{min}}{x_{max} - x_{min}} \quad (1)$$

The normalized pixel value is  $x_{new}$ , the original pixel value is  $x$ , the maximum value of the actual pixel value is  $x_{max}$ , and the minimum value of the initial pixel value is  $x_{min}$ .

### 3.2 Interpolation processing

The original MRA data is three-dimensional, and the dimensionality reduction is displayed for convenience. The image needs to be interpolated to obtain the consistency of three-dimensional accuracy. Here, the following convolutional three-interpolation algorithm is used:

$$f(i+u, j+v) = [A] \times [B] \times [C] \quad (2)$$

$$[A] = [S(u+1) \ S(u+0) \ S(u-1) \ S(u-2)] \quad (3)$$

$$[B] = \begin{bmatrix} f(i-1, j-1) & f(i-1, j+0) & f(i-1, j+1) & f(i-1, j+2) \\ f(i+0, j-1) & f(i+0, j+0) & f(i+0, j+1) & f(i+0, j+2) \\ f(i+1, j-1) & f(i+1, j+0) & f(i+1, j+1) & f(i+1, j+2) \\ f(i+2, j-1) & f(i+2, j+0) & f(i+2, j+1) & f(i+2, j+2) \end{bmatrix} \quad (4)$$

$$[C] = \begin{bmatrix} S(v+1) \\ S(v+0) \\ S(v-1) \\ S(v-2) \end{bmatrix} \quad (5)$$

$$S(x) = \begin{cases} 1 - 2\text{abs}(x)^2 + \text{abs}(x)^3 & , 0 \leq \text{abs}(x) < 1 \\ 4 - 8\text{abs}(x) + 5\text{abs}(x)^2 - \text{abs}(x)^3 & , 1 \leq \text{abs}(x) < 2 \\ 0 & , \text{abs}(x) \geq 2 \end{cases} \quad (6)$$

Using the gray values of 16 points around the sampling point for cubic interpolation, taking into account the influence of gray values of 4 directly adjacent points and the power of gray value change rate to each neighboring

point, the BiCubic function is  $S(x)$   $x$  the distance from the interpolation point to the control point.

Does any point on the image represent a tensor function  $f(i+u, j+v) = [A] \times [B] \times [C]$ , and  $i, j, u, v$  are coordinates (the third direction is a constant value or is measured by the modulus of the third direction tensor),

$[B]$  is a tensor function of the sampling point,  $[A]$  and  $[C]$  are a tensor function of the affected neighborhood.

After changes, the above algorithm adjusts the three directional value arrays. Then, the array values are written into the image data, and the updated image data is obtained through GetArrayFromImage [11-14]. Because it is necessary to compare the experimental machine-generated value with the manual annotated value to reduce the comparison error between the two, 0 interpolation is required, and standard interpolation is needed when only machine processing is done.

### 3.3 Breakpoint detection repair

Gaussian filters can detect and smooth the image in medical images to remove noise and repair minor breakpoints [15,16]. It filters all pixels in the embodiment to be processed through the specified template (convolution, mask) and replaces the scanned pixel value with the weighted average gray matter of the pixel in the neighborhood obtained by calculation. Its functional form is as follows:

$$f(x, y, z) = \frac{1}{(2\pi)^{\frac{3}{2}}} e^{-\frac{x^2+y^2+z^2}{2}} \quad (7)$$

$x, y, z$  represents the pixel values at three corresponding positions in three-dimensional space,  $e$  represents the constant of nature,  $\pi$  and represents PI.

Here, the gaussian\_filter function of Python is used to write a three-dimensional filtering program and perform three-dimensional Gaussian filtering. Selecting a sigma value below 0.4 is best because significant parameters easily blur small blood vessels and cause unclear boundaries. The two-dimensional display of Gaussian filtering images using sigma 0.3 is shown in Figure 4.

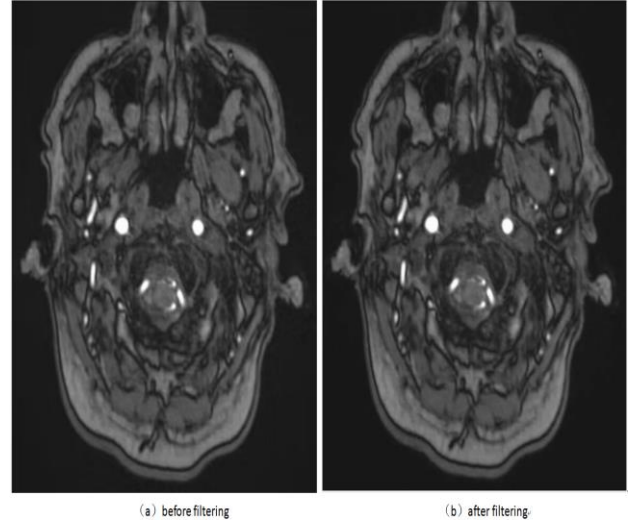


Figure. 4 Comparison of images before and after Gaussian filtering

Through Gaussian filtering of the image, the edge of the image, in this case, is enhanced, and the clarity is more evident in the image comparison display.

### 3.4 Image segmentation

MRA image segmentation must remove other tissues as much as possible, mainly bone tissue. Other soft tissues have little impact on vascular imaging, and the vascular part is preserved to the maximum extent. There are many image segmentation technologies, and the segmentation algorithms include the combination of traditional segmentation algorithms and a variety of segmentation algorithms, such as threshold-based segmentation algorithm, region-based segmentation algorithm (region growth algorithm, split and merge algorithm, watershed algorithm, etc.), and edge detection-based segmentation algorithm. There are also algorithms based on specific tools (segmentation algorithm based on clustering, segmentation algorithm based on wavelet transform, segmentation algorithm based on active contour model, genetic algorithm, etc.) [17-20] and algorithms based on deep learning [8,21-23], etc. Deep learning algorithms are also subdivided into various algorithms. Each of these segmentation algorithms has its advantages and disadvantages. To improve the computing speed and reduce the requirement on hardware computing power without losing accuracy, the traditional watershed algorithm and threshold algorithm are combined to perform MRA image segmentation, as shown in Figure 5. The watershed algorithm is a mathematical segmentation algorithm based on topological theory. It obtains the edge information of the image by calculating the gradient. The algorithm is as follows:

Suppose that for a point  $P(x, y, z)$  on the image, in the range  $P \in D$ ,  $D$  is the image space that conforms to the

function  $u = f(x, y, z)$ , then there is the gradient value at the end  $P$ :

$$\text{gradu} = \frac{\partial u}{\partial x} \vec{i} + \frac{\partial u}{\partial y} \vec{j} + \frac{\partial u}{\partial z} \vec{k} \quad (8)$$

$\vec{i}$ ,  $\vec{j}$ ,  $\vec{k}$  are unit vectors in three directions.

Then, threshold processing is performed on the gradient image to eliminate excessive segmentation caused by small changes in the grayscale. After threshold processing, the segmentation function becomes:

$$g(x, y, z) = \max(\text{gradu}, g\theta) \quad (9)$$

$g\theta$  represents the threshold variable.

The calculation of threshold variables usually includes the maximum inter-class variance method (otsu algorithm), median method, mean method, maximum entropy method (entropy method), iterative method, etc. Here, the complete inter-class variance method is used, and its threshold algorithm is as follows:

$$u_{opt} = u_m = w_0 \times w_1 \times (u_0 - u_1)^2 \quad (10)$$

The interclass variance is  $u_m w_0$  the ratio of foreground voxel number to population prime number,  $w_1$  the ratio of background voxel number to population prime number,  $u_0$  the average gray value of voxel foreground,  $u_1$  and the average gray value of voxel background.

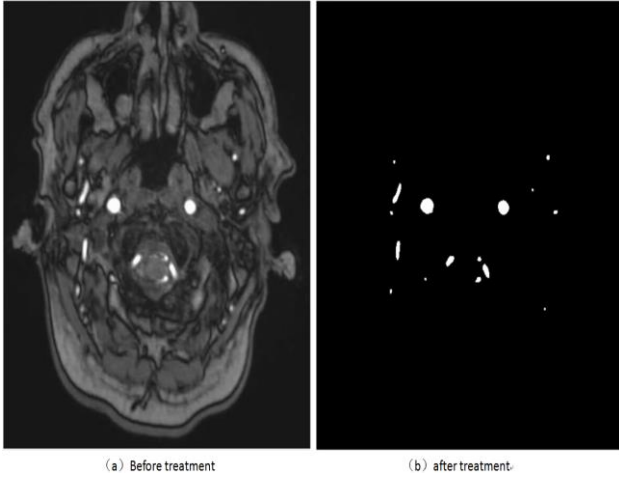
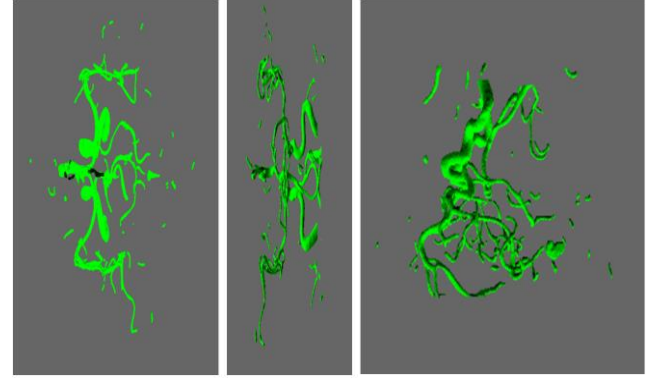


Figure. 5 Comparison of images before and after watershed and threshold correction processing. By performing watershed algorithm segmentation and threshold correction on the filtered image, only the vascular images were retained, while other tissues were removed.

### 3.5 Three-dimensional reconstruction

At present, image 3D reconstruction is divided into two directions: traditional 3D reconstruction based on visual geometry [24-27] and 3D reconstruction based on deep learning [28,29]. Since voxel values of 3D images are

already available here, the SIFT detection algorithm [24] is only needed to obtain feature points in the above photos. Then, the FLANN matching algorithm [25] matches the feature points to different images. Finally, the traditional 3D reconstruction algorithm -SFM algorithm [26] is used to reconstruct the above-processed photos, which can be divided into incremental, global, hybrid, hierarchical, and semantic-based methods of the SFM algorithm [30-32]. A hierarchical algorithm is used for image 3D reconstruction, as shown in Figure 6.



(a) horizontal axis position (b) coronal position (c) sagittal position.

Figure 6 3D Reconstruction Effect of MAR Preprocessed Image

Although the image was segmented using a watershed algorithm and threshold correction, minor omissions may occur due to noise, and skull bones may be difficult to remove due to high pixel values and poor continuity.

To obtain the simple vascular part image, the connectivity analysis of 6 neighborhood areas was performed on the three-dimensional image, and the number, location, surface area, and volume of each part of the connectivity were calculated according to the voxel number. The statistical results are shown in Table 1. According to the obtained data and 3D images, it can be seen that there are still some tiny blood vessels (less than 600 in volume), bone fragments (less than 1700 in volume), and interference noise (less than 100 in book as recommended by clinical experts) that are not connected with large blood vessels. A Gaussian filter must filter out the bone fragments and interference noise. The rest is the blood supply vessels outside the brain that can also be filtered out. After Gaussian filtration, pure blood vessels supplying blood to the brain were reconstructed in three dimensions, as shown in Figure 7.

Table 1 Statistical Table of Connectivity of 3D Modeling of Images after MAR Preprocessing

Table 1-1 Surface area and volume statistics of interference noise location

ID	Center-X	Center-Y	Center-Z	Surface	Volume
0	214.9	1.9	324.2	79.782	44
1	316.5	0.0	164.5	10.121	4
2	351.7	0.9	343.5	51.000	27
3	252.7	71.0	187.5	118.661	61
4	394.7	82.9	215.2	45.125	13
5	393.1	88.7	219.6	114.140	59

6	111.0	137.9	211.8	89.292	37
7	167.4	160.7	227.6	54.962	37

Table 1-2 Surface area and volume statistics of ruptured small blood vessels

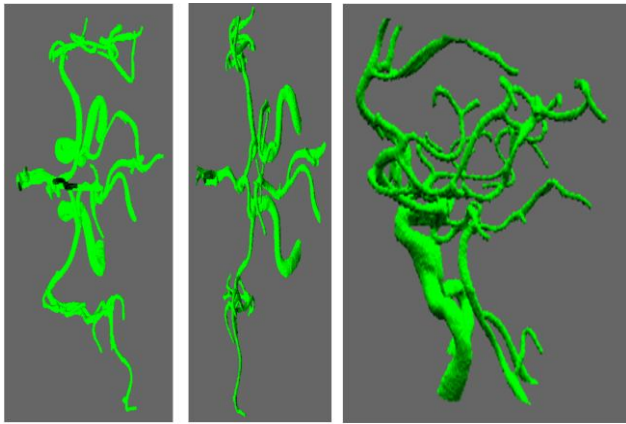
ID	Center-X	Center-Y	Center-Z	Surface	Volume
0	171.1	9.8	342.4	629.976	498
1	180.5	6.3	116.3	235.357	163
2	219.7	1.0	122.1	264.081	344
3	237.9	5.1	104.4	334.902	199
4	238.5	4.0	370.2	308.965	183
5	283.2	0.4	122.6	168.433	170
6	338.5	3.3	110.9	250.995	145
7	361.5	3.7	338.8	204.118	103
8	296.1	134.8	137.8	273.037	143

Table 1-3 Surface area and volume statistics of bone fragment location

ID	Center-X	Center-Y	Center-Z	Surface	Volume
0	321.8	27.6	220.8	1764.15	1257
1	349.9	124.1	229.4	1138.184	1616

Table 1-4 Statistics of surface area and volume of main connected blood vessels

ID	Center-X	Center-Y	Center-Z	Surface	Volume
0	219.5	62.6	233.1	59211.934	90541



(a) horizontal axis position (b) coronal position (c) sagittal position

Figure 7 3D Reconstruction Effect of Filtered Image  
Calculating the volume and position of each discontinuous part of the 3D reconstructed image can eliminate the bone tissue within the skull region and position deviation or noise data suggested by experts. From the perspective of the 3D display, only the vascular part has been preserved.

### 3.6 Skeleton Extraction

The most commonly used 3D skeleton extraction algorithm is the corrosion algorithm [6,33,34], which corrodes the outermost outline from the outer layer and

iterates continuously until the innermost Skeleton of the image remains. The centroid algorithm [7,35-37] is also used in the skeleton extraction of two-dimensional images. In this paper, the centroid algorithm is improved, and the cross-section of blood vessels is located and reshaped by adding average plane calculation. The procedure of the standard plane centroid algorithm is first to regard the blood vessel as a multi-segment curve. The middle plane of the curve and the cross-section of the blood vessel form many small irregular elliptical cross-sections  $D$ , and the centroids of these small elliptical cross-sections are connected to form the Skeleton of the blood vessel. Let a small segment of the blood vessel curve  $t \in [a, b]$   $x = \theta(t)$   $y = \varphi(t)$   $z = \omega(t)$  be derivable in this range, and the derivative  $\theta'(t)$   $\varphi'(t)$

$\omega'(t)$  is not all 0, then the ordinary plane equation at the point  $(x_0, y_0, z_0)(t = t_0)$ : (11)

For each normal plane and the cross-section of blood vessels, according to the plane sheet centroid theory, there is a centroid coincidence:

$$\left\{ \begin{array}{l} \bar{x} = \frac{M_y}{M} = \frac{\sum_{i=1}^n m_i x_i}{\sum_{i=1}^n m_i} \\ \bar{y} = \frac{M_x}{M} = \frac{\sum_{i=1}^n m_i y_i}{\sum_{i=1}^n m_i} \end{array} \right. \quad (12)$$

The particle distributed on the cross-section is  $m_i$

$M = \sum_{i=1}^n m_i$  the total mass of the particle system,

$M_y = \sum_{i=1}^n m_i x_i$  the static moment of the particle system

concerning the Y-axis,  $M_x = \sum_{i=1}^n m_i y_i$  and the static moment of the particle system relating to the X-axis.

Our sections here all meet the conditions of homogeneous flakes, so the above equation (12) can be converted to:

$$\left\{ \begin{array}{l} \bar{x} = \frac{1}{A} \iint_D x d\delta \\ \bar{y} = \frac{1}{A} \iint_D y d\delta \end{array} \right. \quad (13)$$

Where  $A$  is the area of section  $D$  and  $\delta$  is the microregion that meets the requirements of the function.

Python's NumPy library calculates the normal plane and cross-section points determined by the points on the periphery of blood vessels with the threshold value in the

image. Then, the facts on the Skeleton are calculated according to the homogenized slice centroid equation. The positions and voxel values of these points are extracted by changing the voxel values of this point. Make it have a uniform and distinguishable voxel value with other centroid points) to form a new three-dimensional model [37,38], as shown in Figure 8.

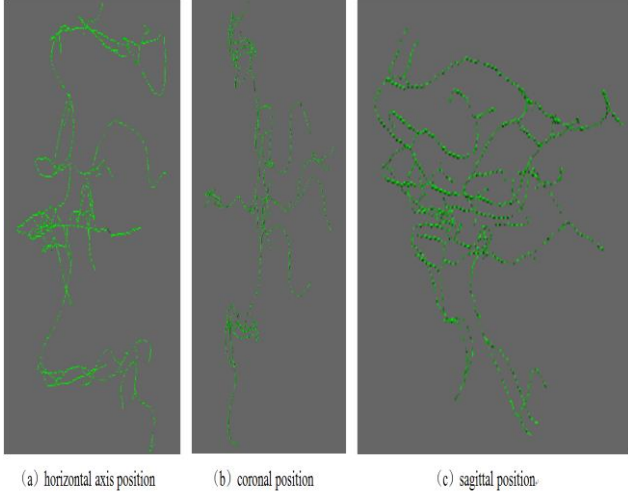


Figure 8 3D skeleton rendering

From the horizontal, coronal, and sagittal positions, it can be seen that the vascular Skeleton extracted through the average plane centroid algorithm has good uniformity and continuity and is complete.

## 4. Experiment and discussion

### 4.1 Data source

Moreover, from a total of 113 normal subjects, the data from the brain magnetic resonance (NMR) public data sets in the <https://public.kitware.com/Wiki/TubeTK/Data> for 100 cases, with the approval of the patient collected 13 subjects of MRA image data in the brain, Acquisition equipment Siemens magnetic resonance instrument model MAGNETOM skyra3.0T, scanning sequence 3D-fl3d1r\_t70, scanning accuracy 0.39mm, layer thickness 0.6mm, image size 512\*464.

### 4.2 Experimental environment

The hardware environment used here is similar to the current mainstream computer, and the software uses a lower open-source stable version, which is convenient for practical application units such as hospitals and medical institutions. Hardware environment: The computer is configured with i7-8520U CPU, 16GDDR3 memory, and 500GSSD hard disk. Software environment: The operating system environment is CentOS6.5, Python version 3.6, torch version 1.7, and other dependency packages and libraries.

### 4.3 Verification method

#### 4.3.1 Efficiency Comparison Experiment

The efficiency of 3D modeling and skeleton extraction has a great relationship with the software and hardware configuration. The size, accuracy, and thickness of the sweeping layer of the image all affect the operation efficiency. Under the above software and hardware configuration environment and sample data, the maximum CPU usage of the 3D modeling machine is 10%, the minimum 0.5%, the maximum memory consumption is 4%, the minimum 1.5% and the average time is 48ms; the maximum CPU usage of the skeleton extraction is 8%, the minimum memory consumption is 1.6%, the maximum memory consumption is 3%, the minimum memory consumption is 0.7%, and the average time is 34ms. The skeleton extraction efficiency pairs under similar conditions are shown in Table 2.

Table 2 Comparison of 3D Image Skeleton Extraction Efficiency

ID	references	methods	efficiency
1	Bitter et al.,2001 <sup>[39]</sup>	3D erosion algorithm	21.1mins
2	Jin et al.,2016 <sup>[7]</sup>	3D erosion algorithm	82sec

#### 4.3.2 Accuracy analysis

By taking the key points in the three positions of coronal position, disfigures-position, and axial position of the image, the machine automatically selects the endpoint specified by the Skeleton, as shown in Figure 9; the manual selection is verified through communication with clinical experts, as shown in Figure 10; and then the original data position measurement through the subject data and the corresponding position measurement after the formation of the vascular Skeleton is verified. Based on the structure of the blood vessel image, the branch intersection points and the endpoints of each segment of blood vessels (that is, the breakpoint) are selected as the key points. The critical point locations measured in the original image (Table 3) are compared with the corresponding points of the blood vessel skeleton (Table 4). If the fitting probability of the position points exceeds 97% of the experimental design, it is considered that the experimental requirements are met. The expected probability is calculated as follows:

$$P = \left(1 - \frac{\sum_{i=1}^n p_i}{n}\right) \times 100\% = \left(1 - \frac{1}{n} \sum_{i=1}^n \frac{|A_i|}{|B_i|}\right) \times 100\% \quad (14)$$

$P$  represents the probability of fitting the attempted image skeleton,  $p_i$  the probability of fitting the critical point,  $n$  the selected vital point,  $A_i$  the difference vector of the vital point, and  $B_i$  the actual vector value of the critical point (the skeleton position vector is used here).

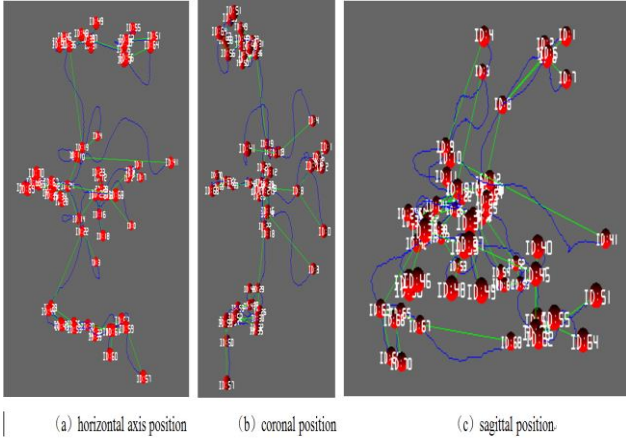


Figure 9 Selection of Key Points for 3D Skeleton  
All key points that need to be verified are selected at the top and fork positions of the Skeleton. The advantage of this selection method is that the work is easy to determine, manual annotation is more accessible, and it is convenient for later comparison and verification.

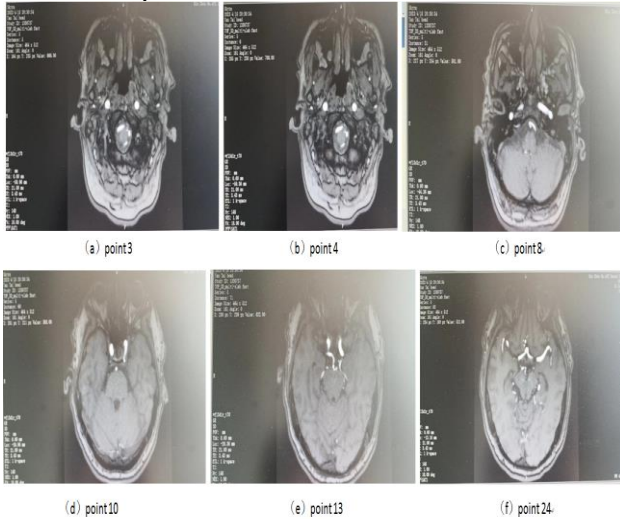


Figure10 Selection of Key Points for Manual Confirmation

Experts on the original image complete the critical points for manual confirmation of the image, and parts are selected for display through shooting.

Using Python's statistics function, the branch intersection points and the endpoints of each segment of blood vessels are automatically calculated as the coordinates of critical issues. Then, the corresponding vital points are found and marked on the original image by manual means, and the coordinates of these manual standard points are given. The three-dimensional scatter diagram of the fitting degree formed by the two coordinate points is shown in Figure 11.

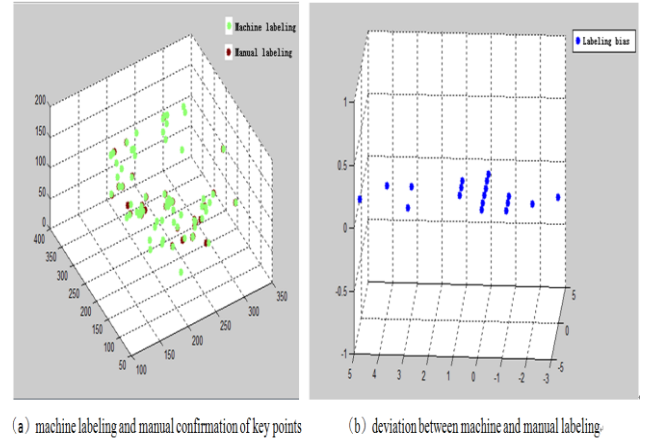


Figure11 Machine annotation and manual confirmation of key point fitting scatter plots

By analyzing the data using Matlab2014a and creating a scatter plot, the critical points annotated by the machine and manually are consistent, and the expected values meet the requirements of the experimental design.

The coordinates of the original image are converted after processing, and corresponding transformations are required when calculating the coordinates of the critical points of the machine and the manual. Suppose that the coordinate axis of the three-dimensional image is (X, Y, Z). The coordinate after transformation is (X', Y', Z'), according to the coordinate relationship between the original image and the converted image; the actual image

coordinate  $M(x, y, z)$  is converted  $M'(x', y', z')$  through normalization, difference processing, and other preprocessing processes. Since the original image starting point is  $M_i(0,0,1)$ , the image starting point is  $M'_i(0,0,0)$  after the conversion, that is, the starting point of the coordinate has shifted, the starting point of the coordinate moves parallel along the Z axis, the displacement vector is 1, and there is  $M'(x' = z, y' = x, z' = y - 1)$  in the conversion process.

That is to say, from the original image coordinate to the converted image coordinate also occurs rotation, with the Y axis as the rotation axis, the vertical plane rotates 90° clockwise, the actual Z axis becomes the present X axis, and then with the current X axis as the rotation axis, rotate the X-axis normal plane 90° counterclockwise, the Y axis becomes the present Z axis. The X axis becomes the present Y axis. Then, according to the above equation (14), the P values of image skeleton line fitting for all subjects were calculated to be the maximum 99.72% and the minimum 99.35%, respectively. The expected

probability  $[40,41] P_E = 99.61\%$  is obtained by calculating the average value. The 3D skeleton extraction accuracy pairs under similar conditions are shown in Table 3.

Table 3 Comparison of accuracy of 3D image skeleton extraction

ID	references	methods	accuracy
----	------------	---------	----------

1	Lebre al.,2018 <sup>[42]</sup>	et	3D algorithm	erosion	0.97
2	Merveille al.,2017 <sup>[43]</sup>	et	3D algorithm	erosion	0.90

## 5. Closing remarks

Under the same hardware and software conditions, the improved average plane centroid algorithm has apparent advantages in efficiency and accuracy compared with the corrosion algorithm and machine learning algorithm to extract the three-dimensional Skeleton of MRA blood vessels. This method's defect is that the early stage preprocessing process will cause specific errors. With the development of artificial intelligence technology, the machine processing speed increases. In addition, in the case of using a large number of samples for deep learning, the machine learning algorithm has more room for improvement. The next step that must be verified is improving the hardware configuration. The effect will be better if the machine learning algorithm is combined with the average plane centroid algorithm to extract the Skeleton of three-dimensional images. Through the use of three-dimensional vascular Skeleton, the cross-sectional area of each section of blood vessel can be reshaped, the changes of vascular cross section can be more intuitively understood, the narrow and dilated weak areas of blood vessels can be accurately located, and the relationship between brain region and changes in cerebrovascular blood supply can be analyzed in combination with the brain structure data of MRIT1, which is of great significance for guiding the prevention of cerebrovascular diseases in patients, especially in the middle-aged and elderly.

## 6. Funding

This work is supported by Shandong Province Major Science and Technology Innovation Project (2018CXGC1501); Binzhou Medical College's 2022 Xu Rongxiang Fund Project (BY2022XR03).

## References

- [1] THOMAS KE, FOTAKI A, BOTNAR RM, FERREIRA VM. Imaging Methods: Magnetic Resonance Imaging[J]. *Circ Cardiovasc Imaging*. 2023;16(1):e014068.
- [2] THAYABARANATHAN T, KIM J, CADILHAC DA, et al. Global stroke statistics 2022[J]. *International Journal of Stroke*. SEP 2022; 17(9):946-956.
- [3] LIU L, CHEN W, ZHOU H, et al. Chinese Stroke Association guidelines for clinical management of cerebrovascular disorders: Executive summary and 2019 update of clinical management of ischaemic cerebrovascular diseases[J]. *Stroke Vasc Neurol*. 2020;5(2):159-176.
- [4] GBD 2016 Causes of Death Collaborators. Global, regional, and national age-sex specific mortality for 264 causes of death, 1980-2016: a systematic analysis for the Global Burden of Disease Study 2016 [published correction appears in *Lancet*. 2017 Oct 28;390(10106):e38]. *Lancet*. 2017;390(10100):1151-1210.
- [5] NIU J, RAN Y, CHEN R, et al. Use of PETRA-MRA to assess intracranial arterial stenosis: Comparison with TOF-MRA, CTA, and DSA. *Front Neurol*. 2023;13:1068132.
- [6] MASSEY RM, WARREN OJ, SZCZEKLIC M, et al. Skeletonization of radial and gastroepiploic conduits in coronary artery bypass surgery[J]. *J Cardiothorac Surg*. 2007;2:26.
- [7] JIN D, IYER KS, CHEN C, et al. A Robust and Efficient Curve Skeletonization Algorithm for Tree-Like Objects Using Minimum Cost Paths.*Pattern Recognit Lett*. 2016;76:32-40.
- [8] WAGNER MG. Real-Time Thinning Algorithms for 2D and 3D Images using GPU processors. *J Real-Time Image Process*. 2020;17(5):1255-1266.
- [9] YANG H, ZHAO XY, WANG L. Review of Data Normalization Methods[J]. *Computer Engineering and Applications*, 2023,59(3):13-22.
- [10] VAN DEN BERGE K, CHOU HJ, ROUX DE BÉZIEUX H, et al. The normalization benchmark of ATAC-seq datasets shows the importance of accounting for GC-content effects[J]. *Cell Rep Methods*. 2022,2(11):100321.
- [11] ZHANG XJ. SPLINE INTERPOLATING OPERATORS AND THE BEST APPROXIMATION OF LINEAR FUNCTIONALS IN  $W_2^m$  SPACES[J]. *MATHEMATICA NUMERICA SINICA*, 2002,24(2):129-136.
- [12] ZHU J. Application of Convolutional Triple Interpolation Algorithm in Processing Medical Images[J]. *China Computer & Communication*, 2021,33(23):77-79+83.
- [13] TAVOOSI J, ZHANG C, MOHAMMADZADEH A, et al. Medical Image Interpolation Using Recurrent Type-2 Fuzzy Neural Network[J].*Front Neuroinform*. 2021;15:667375.
- [14] ZUO C, QIAN J, FENG S, et al. Deep learning in optical metrology: a review [published correction appears in *Light Sci Appl*. 2022 Mar 27;11(1):74].*Light Sci Appl*. 2022;11(1):39.
- [15] XIAO C, LI F, ZHANG DY. Image Inpainting Detection Based on High-Pass Filter Attention Network[J]. *Computer Systems Science and Engineering* 2022, 43(3):1145-1154.
- [16] ZHANG F, XI QY, LI QX, et al. Feasibility of removing manual marks on ultrasonic images and repairing images based on double gradient combined with improved Criminisi algorithm[J]. *Chin J Med Imaging Technol*, 2023, 39(03):429-434.
- [17] SASMAL B, DHAL KG. A survey on utilizing Superpixel image for clustering-based image segmentation [published online ahead of print, 2023 Mar 8].*Multimed Tools Appl*. 2023;1-63.
- [18] KORNILOV A, SAFONOV I, YAKIMCHUK I. A Review of Watershed Implementations for Segmentation of Volumetric Images. *J Imaging*. 2022;8(5):127.
- [19] KUBICEK J, VARYSOVA A, CERNY M, et al. Performance and Robustness of Regional Image

- Segmentation Driven by Selected Evolutionary and Genetic Algorithms: Study on MR Articular Cartilage Images[J]. *Sensors (Basel)*. 2022;22(17):6335.
- [20] ZHANG W, WU Y, YANG B, et al. Overview of Multi-Modal Brain Tumor MR Image Segmentation. *Healthcare (Basel)*. 2021;9(8):1051.
- [21] KAR A, PETIT M, REFAHI Y, et al. Benchmarking of deep learning algorithms for 3D instance segmentation of confocal image datasets[J]. *PLoS Comput Biol*. 2022; 18(4):e1009879.
- [22] CHEN C, QIN C, QIU H, et al. Deep Learning for Cardiac Image Segmentation: A Review[J]. *Front Cardiovasc Med*. 2020;7:25. Published 2020 Mar 5. doi:10.3389/fcvm.2020.00025
- [23] FU Y, LEI Y, WANG T, et al. A review of deep learning-based methods for medical image multi-organ segmentation[J]. *Phys Med*. 2021;85:107-122.
- [24] BRUNO A, ARDIZZONE E, VITABILE S, MIDIRI M. A Novel Solution Based on Scale Invariant Feature Transform Descriptors and Deep Learning for the Detection of Suspicious Regions in Mammogram Images. *J Med Signals Sens*. 2020;10(3):158-173.
- [25] BITTREMIEUX W, MEYSMAN P, NOBLE WS, LAUKENS K. Fast Open Modification Spectral Library Searching through Approximate Nearest Neighbor Indexing. *J Proteome Res*. 2018;17(10):3463-3474.
- [26] NIELSEN MS, NIKOLOV I, KRUSE EK, GARNÆS J, MADSEN CB. Quantifying the Influence of Surface Texture and Shape on Structure from Motion 3D Reconstructions. *Sensors (Basel)*. 2022;23(1):178.
- [27] ZIEGLER JP, OYER SL. Prelaminated paramedian forehead flap for subtotal nasal reconstruction using three-dimensional printing[J]. *BMJ Case Rep*. 2021; 14(1):e238146.
- [28] PENG W, PENG Z, TANG P, et al. Review of Plastic Surgery Biomaterials and Current Progress in Their 3D Manufacturing Technology. *Materials (Basel)*. 2020;13(18):4108.
- [29] TARASSOLI SP, SHIELD ME, ALLEN RS, et al. Facial Reconstruction: A Systematic Review of Current Image Acquisition and Processing Techniques. *Front Surg*. 2020;7:537616.
- [30] KANEDA A, NAKAGAWA T, TAMURA K, et al. A proposal of a new automated method for SfM/MVS 3D reconstruction through comparisons of 3D data by SfM/MVS and handheld laser scanners[J]. *PLoS One*. 2022;17(7):e0270660.
- [31] GAO L, ZHAO Y, HAN J, et al. Research on Multi-View 3D Reconstruction Technology Based on SFM[J]. *Sensors (Basel)*. 2022;22(12):4366.
- [32] NIELSEN MS, NIKOLOV I, KRUSE EK, et al. Quantifying the Influence of Surface Texture and Shape on Structure from Motion 3D Reconstructions[J]. *Sensors (Basel)*. 2022;23(1):178.
- [33] ZHANG J, WU F, CHANG W, et al. Techniques and Algorithms for Hepatic Vessel Skeletonization in Medical Images: A Survey[J]. *Entropy (Basel)*. 2022;24(4):465.
- [34] SILVERSMITH W, ZLATESKI A, BAE JA, et al. Igneous: Distributed dense 3D segmentation meshing, neuron skeletonization, and hierarchical downsampling[J]. *Front Neural Circuits*. 2022;16:977700.
- [35] WU J, TURNER N, BAE JA, et al. RealNeuralNetworks.jl: An Integrated Julia Package for Skeletonization, Morphological Analysis, and Synaptic Connectivity Analysis of Terabyte-Scale 3D Neural Segmentations [J]. *Front Neuroinform*. 2022;16:828169.
- [36] YUAN X, TRACHTENBERG JT, POTTER SM, et al. MDL-constrained 3-D grayscale skeletonization algorithm for automated extraction of dendrites and spines from fluorescence confocal images[J]. *Neuroinformatics*. 2009;7(4):213-232.
- [37] YU H, ZHANG X, WANG Z, et al. Research on the Pose Error Compensation Technology for the Mass and Centroid Measurement of Large-Sized Aircraft Based on Kinematics[J]. *Sensors (Basel)*. 2023;23(2):701.
- [38] LUKIĆ T, BALÁZS P. Limited-view binary tomography reconstruction assisted by shape centroid[J]. *Vis Comput*. 2022;38(2):695-705.
- [39] Bitter I, Kaufman AE, Sato M. Penalized-distance volumetric skeleton algorithm. *IEEE Trans Visualization Computer Graphics*. 2001;7:195-206.
- [40] LIN WH, GARDNER JL, WU SW. Context effects on probability estimation[J]. *PLoS Biol*. 2020;18(3):e3000634.
- [41] YAMADA H, IMAIZUMI Y, MATSUMOTO M. Neural Population Dynamics Underlying Expected Value Computation[J]. *J Neurosci*. 2021;41(8):1684-1698.
- [42] LEBRE MA, VACANT A, GRAND-BROCHIER M, et al. Automatic 3-D skeleton-based segmentation of liver vessels from MRI and CT for Chouinard representation[C]// Proceedings of the 2018 25th IEEE International Conference on Image Processing (ICIP); Athens, Greece. 7-10 October 2018; pp. 3523-3527.
- [43] MERVEILLE O, NAEGEL B, TALBOT H, et al. 2D filtering of curvilinear structures by ranking the orientation responses of path operators (RORPO)[J]. *Image Processing On Line*, 2017, 7:246-261.